Research Square

Preprints are preliminary reports that have not undergone peer review.
They should not be considered conclusive, used to inform clinical practice,
or referenced by the media as validated information.

An Upward-Continuation-Based Framework for Subsurface Structural Reconstruction from Gravity Anomalies

Ako Alipour

farn1366@yahoo.com

IASBS: Institute for Advanced Studies in Basic Sciences https://orcid.org/0000-0002-3378-1750

Khalil Motaghi

IASBS: Institute for Advanced Studies in Basic Sciences

Zahra Mousavi

IASBS: Institute for Advanced Studies in Basic Sciences

Research Article

Keywords: Gravity anomaly interpretation, upward continuation, spectral decomposition, analytic signal, normalized full gradient, UCRD

Posted Date: July 1st, 2026

DOI: https://doi.org/10.21203/rs.3.rs-10035074/v1

License: This work is licensed under a Creative Commons Attribution 4.0 International License.
Read Full License

An Upward-Continuation-Based Framework for Subsurface Structural Reconstruction from Gravity Anomalies

Ako Alipour[1*], Khalil Motaghi[1], Zahra Mousavi[1]

[1] Department of Earth Sciences, Institute for Advanced Studies in Basic Sciences (IASBS), Zanjan 45137-66731, Iran

Abstract

In this study, we introduce the Upward Continuation Restriction to Decomposition (UCRD) framework, an upward-continuation-based decomposition approach for reconstructing subsurface structural geometry directly from Bouguer gravity anomalies. The method applies multi-level upward continuation using exponentially increasing continuation heights to separate the gravity field into restricted wavelength levels associated with different depth intervals. These levels are subsequently transformed through a three-dimensional analytic signal and a scale-adaptive normalization procedure to generate scaled restricted wavelength (SRWL) representations that preserve anomaly polarity, enhance structural continuity, and provide physically interpretable images of gravity-source geometry.

To complement structural reconstruction with depth information, UCRD is integrated with the Normalized Full Gradient (NFG) method. In this combined framework, UCRD provides geometric characterization of subsurface structures, whereas NFG supplies quantitative depth constraints. The methodology is validated using three synthetic gravity models of increasing complexity, including isolated bodies with varying density contrasts, overlapping prisms, and laterally extensive stepped structures. The results demonstrate that UCRD successfully delineates horizontal and vertical structural geometries over a wide range of source depths, while NFG reliably identifies corresponding depth positions even in geometrically complex environments.

The proposed UCRD–NFG workflow operates directly on gravity data without requiring inversion, prior geological information, or computationally intensive optimization procedures. Consequently, it provides an efficient and model-independent framework for gravity interpretation and can serve as a valuable preliminary characterization tool for subsequent forward modelling, inversion, and integrated geophysical investigations.

Key Words

Gravity anomaly interpretation, upward continuation, spectral decomposition, analytic signal, normalized full gradient, UCRD

1. Introduction

Gravity data interpretation remains one of the most fundamental and widely applied approaches for investigating subsurface density heterogeneity because the observed gravity field reflects spatial variations in subsurface density contrasts across a wide range of scales and its applicability across a broad range of geological environments (Balmino et al., 1999; Pail, 2023), from sedimentary basin analysis to lithospheric-scale investigations (Ismail-Zadeh et al., 2020). The observed gravity field reflects the cumulative response of density contrasts within the Earth, providing indirect but spatially continuous constraints on subsurface structure. Gravity measurements do not directly sample geological materials; instead, they detect variations in the gravitational field arising from density heterogeneities at depth. Consequently, gravity data provide an efficient means of investigating subsurface structural configurations over regional to continental scales (Blakely, 1995; Hinze et al., 2012), particularly in areas where direct observations are limited or unavailable.

Despite these advantages, gravity interpretation remains fundamentally non-unique because substantially different density distributions can generate similar anomaly responses (Blakely, 1995). This inherent ambiguity has motivated the development of a wide range of interpretation methodologies, including forward modelling, inversion, transformation-based enhancement, and more recently machine-learning approaches. Inversion techniques aim to estimate subsurface density distributions from observed gravity anomalies (Oldenburg, 1974; Li & Oldenburg, 1998; Zhao et al., 2018; Zhang et al., 2018), while joint inversion strategies incorporate complementary geophysical information to improve model reliability (Gallardo & Meju, 2004; Lelièvre et al., 2012; Lin & Zhdanov, 2018; Ming et al., 2024). Similarly, forward-modelling approaches reconstruct subsurface geometry by matching observed anomalies with assumed structural configurations (Talwani & Ewing, 1960; Nagy, 1966), but their effectiveness depends strongly on prior geological constraints, model parameterization, and assumptions regarding structural complexity (Zhdanov, 2002; Farquharson & Oldenburg, 2004; Bosch et al., 2010; Moorkamp et al., 2011).

To reduce reliance on prior information, numerous transformation-based methods have been developed to extract structural information directly from gravity data. Classical approaches include upward continuation (Nettleton, 1954; Jacobsen, 1987), polynomial surface fitting (Agocs, 1951; Simpson, 1954), spectral analysis (Spector & Grant, 1970), wavelet decomposition (Fedi & Quarta, 1998; Xu et al., 2009), and nonlinear filtering (Keating & Pinet, 2011). Among these methods, the analytic signal transformation has become one of the most widely used enhancement techniques because it emphasizes the magnitude of gravity-field gradients independently of anomaly polarity, making it particularly effective for structural mapping and source-boundary delineation (Nabighian, 1972; Debeglia & Corpel, 1997; Nabighian et al., 2005a; Doo et al., 2009).

Another important gradient-based approach is the normalized full gradient (NFG) method, originally developed by Berezkin and co-workers (Berezkin & Buketov, 1965; Berezkin, 1967, 1973, 1988) and subsequently refined for potential-field interpretation (Elysseieva & Pašteka, 2018; Alipour et al., 2023a, 2023b; Wang et al., 2025). Recent developments include iterative structural reconstruction approaches such as ITRESC (Florio, 2018) and the growing application of machine-learning techniques for gravity interpretation (e.g., Meng et al., 2025; Zhanakulova et al., 2025). Alongside these advances, the NFG method has gained renewed attention as a powerful approach for enhancing structural features and characterizing source depths in potential-field data (Elysseieva & Pašteka, 2018; Alipour et al., 2023a, 2023b; Wang et al., 2025).

By analyzing normalized gradient responses, NFG improves the identification of structural boundaries and provides valuable information regarding source depth. Nevertheless, the method remains fundamentally gradient-based, and therefore primarily responds to spatial variations in the anomaly field rather than directly representing density polarity or the complete geometry of the causative body. Bodies with opposite density contrasts may produce similar normalized responses, while laterally extensive structures often exhibit diminished responses over their central regions. Consequently, NFG and related gradient-based techniques are highly effective for detecting edges and estimating depth, but they do not directly reconstruct the full spatial geometry of subsurface structures (Alipour et al., 2023b).

More broadly, most existing gravity-processing techniques focus on anomaly enhancement, boundary detection, wavelength separation, or density estimation. Although these approaches provide valuable interpretational information, relatively few methods are specifically designed to reconstruct the overall structural geometry of gravity-source bodies directly from gravity anomalies while preserving anomaly polarity and requiring neither inversion nor external

92 geological constraints. This limitation motivates the development of a complementary framework
93 capable of transforming gravity anomalies into physically interpretable representations of
94 subsurface structural geometry.

95 To address this challenge, we introduce the Upward Continuation Restriction to Decomposition
96 (UCRD) framework, an upward-continuation-based decomposition methodology for
97 reconstructing subsurface structural geometry directly from gravity anomaly data. The method
98 applies controlled multi-level upward continuation to separate the gravity field into restricted
99 wavelength levels associated with different spatial scales and depth ranges. A three-dimensional
100 analytic signal transformation is subsequently applied to each decomposed level, followed by a
101 scale-adaptive normalization procedure that restores physical units (mGal), preserves anomaly
102 polarity, and enhances structural continuity. The resulting scaled restricted wavelength (SRWL)
103 representations provide physically interpretable images that facilitate direct visualization of
104 subsurface structural geometry.

105 Because potential-field (gravity) data suffer from inherent non-uniqueness in depth estimation,
106 structural reconstruction through UCRD is complemented by the normalized full gradient (NFG)
107 method. Within this integrated framework, UCRD provides geometric characterization of
108 subsurface structures, whereas NFG supplies independent depth constraints. The combined
109 methodology therefore enables simultaneous interpretation of structural geometry and source
110 depth within a unified and computationally efficient workflow.

111 The proposed framework is evaluated using three synthetic gravity models representing a range of
112 structural complexities, including isolated bodies, overlapping structures, and laterally extensive
113 sources. These tests assess the capability of the UCRD–NFG framework to reconstruct structural
114 geometry, resolve spatial complexity, and characterize source depth. The results demonstrate that

the proposed methodology provides a practical and computationally efficient approach for gravity interpretation and can serve as a valuable preliminary characterization tool for subsequent forward modelling, inversion, and integrated geophysical investigations.

2. Methods

The structural reconstruction component of this study follows the multi-level gravity interpretation framework introduced in Alipour et al. (2025 preprint), while the depth-constraint analysis is independently based on the NFG development of Alipour et al. (2023b).

We adopt a right-handed Cartesian coordinate system (x, y, z), with x and y representing the horizontal directions, and z positive upward from the geoid. Each gravity measurement is located at $P_i = (x_i, y_i, z_i)$ with z_i equal to the station elevation above the geoid. We retain true z_i (no flattening to $z = z_0$) to preserve topographic sensitivity. Subsurface sources follow the same convention, a density source at depth d beneath station i is positioned a $z_d = z_i - d$ (< 0).

2.1 Multi-Level Upward Continuation and Frequency Band Decomposition

We isolate short-wavelength (shallow) and long-wavelength (deep) contributions by performing multiple upward continuations (Blakely, 1995). Let $U_0(x, y) = U(x, y, z_i)$ be the Bouguer anomaly sampled at the true station elevations z_i. The upward continuation of a field U from height z_i to $z_i + \Delta z$ in the wavenumber domain is (Henderson & Zietz, 1949; Henderson, 1970; Blakely, 1995; Ravat, 2007):

$$U(x, y, z_i + \Delta z) = \iint U\big(k_x, k_y, z_i\big) e^{-k\Delta z} e^{i(k_x x + k_y y)} dk_x dk_y \quad (1)$$

where Δz is the continuation height ($\Delta z > 0$ upward) and $k = \sqrt{k_x^2 + k_y^2}$ is the radial wavenumber.

The first upward continuation U_1 is computed with a vertical increment Δz_1. We choose Δz_1 to balance horizontal sampling and noise level; it must not be too small relative to the horizontal sampling interval to avoid aliasing (Blakely, 1995), and it should not amplify reduction errors (Heath, 2018).

The first restricted wavelength level is then:

$$RWL_1(x, y) = U_0(x, y) - U_1(x, y) \quad (2)$$

which isolates the shortest spatial wavelengths (shallowest sources).

To efficiently investigate progressively deeper source levels, the vertical spacing between successive continuation heights is increased according to the empirical relationship:

$$\Delta z_n = \Delta z_1 \exp(n - 1), n = 2, \dots, N \quad (3)$$

The suggested empirical relationship (Eq.3) provides a smooth and efficient progression between two regimes, preserving sensitivity to shallow structures while avoiding unnecessary oversampling at greater depths. Dense sampling is preferred at shallow levels where short-wavelength anomalies contain significant structural detail, whereas progressively larger spacing becomes sufficient at greater heights as the field becomes increasingly dominated by long-wavelength regional components. The process stops ($n = N$) when the amplitude of the deepest average RWL_N falls below average response of RWL_1.

At each step, the continued field is computed in the Fourier domain (We define for $n = 1 \dots N$):

$$U_n(x,y) = \mathcal{F}^{-1}\{\mathcal{F}[U_{n-1}](k_x,k_y)\exp(-\|\mathrm{k}\|\Delta z_n)\}, \|\mathrm{k}\| = \sqrt{k_x^2+k_y^2} \quad (4)$$

and the corresponding restricted level is:

$$RWL_n(x,y) = U_{n-1}(x,y) - U_n(x,y) \quad (5)$$

Each RWL_n isolates anomalies whose dominant wavelengths correspond to distinct depth intervals. Although perfect spectral separation is unattainable due to band overlap and finite-grid effects (Blakely, 1995; Prabhu, 2014), zero-phase cosine tapering and symmetric domain padding minimize cross-band leakage and edge artifacts (Prabhu, 2014). UCRD reconstructs the full 3D anomaly field by stacking these band-limited layers from shallowest to deepest.

2.2 Analytical Signal and Scale Normalization

To enhance lateral structural expression, we apply the three-dimensional analytic signal transformation (Nabighian, 1972; Nabighian et al., 2005a; Debeglia & Corpel, 1997; Doo et al., 2009) to each RWL_n:

$$AS_n(x,y)[\frac{mGal}{km}] = \sqrt{(\partial_x RWL_n(x,y))^2 + \left(\partial_y RWL_n(x,y)\right)^2 + (\partial_z RWL_n(x,y))^2} \quad (6)$$

The analytic signal amplitude is always positive and peaks at density contrast edges. To enable inter-level comparison, we apply a scale normalization. First, compute the spatial mean of AS_n:

$$\overline{AS_n}[\frac{mGal}{km}] = mean\{AS_{\mathrm{n}}(x,y)\} \quad (7)$$

Then define a level-specific scale factor based on the dynamic range of RWL_n:

$$SF_n[mGal] = \frac{max(RWL_n(x,y))[mGal] - min\left(RWL_n(x,y)\right)[mGal]}{max\left(\frac{AS_n(x,y)}{\overline{AS_n}}\right)[1] - min\left(\frac{AS_n(x,y)}{\overline{AS_n}}\right)[1]} \quad (8)$$

Finally, the scaled restricted wavelength level is:

$$SRWL_n(x,y)[mGal] = sgn\big(RWL_n(x,y)\big)[1] \cdot \left(\frac{AS_n(x,y)}{\overline{AS_n}}[1] \cdot SF_n[mGal]\right) \quad (9)$$

This procedure restores the physical units of the gravity field based on scaling factor ($SF_n[mGal]$) and preserves anomaly polarity by combining the normalized analytic signal amplitude ($\frac{AS_n(x,y)}{\overline{AS_n}}$) with the sign of the original band-limited anomaly ($sgn\big(RWL_n(x,y)\big)$). The resulting SRWLn maps capture both magnitude and direction of lateral density contrasts at each depth level, enhancing the visibility of features that may be obscured in the raw gravity field.

Following decomposition of the gravity field into (SRWLn) components, the complete set of SRWL levels is integrated to reconstruct the geometry of the causative anomalous bodies. Each SRWL map corresponds to a different upward continuation height and therefore reflects a distinct stage of spectral attenuation, with shallow-source effects progressively reduced as continuation height increases. When analyzed collectively, these maps provide a pseudo-three-dimensional representation of the anomaly evolution, allowing the lateral continuity, structural configuration, and relative persistence of anomalous features to be examined across successive continuation levels. Although upward continuation does not yield direct depth information, the progressive suppression of short-wavelength components enables deeper source contributions to become increasingly prominent relative to shallow anomalies. Horizontal maps and vertical sections constructed from the ensemble of SRWL levels therefore provide a useful framework for visualizing and interpreting subsurface geometry.

2.3 NFG

The NFG method is based on the downward analytical continuation of gravity data. Analytical continuation enhances the expression of subsurface density contrasts and structural features that may be poorly resolved in the observed gravity field (Aydin, 2007). As the gravity field is

196 analytically continued downward, characteristic variations develop in the vicinity of the causative
197 masses, providing additional information on source geometry and location (Berezkin, 1988;
198 Aydin, 1997a). In practice, the normalized full gradient (NFG) is preferred to the continued gravity
199 field itself because of its greater stability and its ability to delineate the positions of anomalous
200 source bodies more effectively.

201 The gravity anomaly data along the x-axis can be expressed as a sum of sine and cosine functions
202 (Ciancara & Marcak, 1979; Bracewell, 1984; Blakely, 1995; Pasteka, 2000) and computed in the
203 frequency domain using a Fourier-series formulation following Berezkin (1973). In this approach,
204 the superposition of harmonic sine and cosine components, allowing spatial derivatives and
205 continuation operators to be evaluated efficiently. Consequently, the NFG operator can be applied
206 to gravity anomaly data following downward analytical continuation. In the frequency domain, the
207 downward continuation process is performed at each continuation level z using a Fourier-series
208 representation, yielding:

209 $$\Delta g(x,z) = \sum_{n=1}^{N} B_n \sin\left(\frac{n\pi x}{L}\right) exp\left(\frac{n\pi z}{L}\right) \quad (10)$$

210 The Fourier series expresses a periodic function in terms of its harmonic components, where B_n is
211 the Fourier coefficients and n denotes the harmonic number (Bracewell, 1984; Blakely, 1995).
212 Using Eq. (10), the gravity anomaly field, $\Delta g(x,z)$, can be analytically continued to positions
213 above and below a specified reference plane along the z-axis (Berezkin & Buketov, 1965;
214 Berezkin, 1973; Zeng et al., 2002).

215 $$B_n = \frac{2}{L}\int_0^L \Delta g\,(x,0)\sin\left(\frac{n\pi x}{L}\right) dx \quad (11)$$

When a sine Fourier-series representation is employed, the interpreted function must satisfy zero boundary conditions at the profile endpoints ($x = 0$ and $x = L$) (Elysseieva & Pašteka, 2018). To satisfy this requirement, a linear trend is commonly removed to avoid edge discontinuities; however, this procedure may also suppress meaningful regional components of the gravity field. Bouguer gravity anomalies inherently contain both short-wavelength contributions associated with shallow sources and long-wavelength components related to deeper crustal and lithospheric structures. To preserve the full wavelength content while mitigating edge effects, the NFG method is applied together with a signal-mirror extension strategy, which avoids artificial discontinuities without removing long-wavelength information (Alipour et al., 2023b)

Evaluation (11) is performed using numerical integration. A stable numerical scheme based on the trapezoidal rule has been adopted in subsequent implementations of the NFG approach (Dondurur, 2005; Aydin, 2007; Aghajani et al., 2009a). Within this framework, a central challenge is the selection of the optimal number of harmonics (N), which directly controls the stability and resolution of the harmonic response. In the conservative formulation of the normalized full gradient (NFG) method, the optimal number of harmonics (N) is determined using N-value analysis (Zeng et al., 2012). The concept of N-restricted processing has been extensively investigated in previous studies (Aydin, 1997a; Berezkin, 1988; Dondurur, 2005; Sindirgi et al., 2008; Aghajani et al., 2009a, 2009b, 2011; Oruç, 2011; Zhang & Meng, 2015; Xuan et al., 2018, Elysseieva & Pašteka, 2018, Alipour et al., 2023b).

Several strategies have been proposed for estimating N. Aghajani et al. (2009a, 2009b, 2011) and Xuan et al. (2018) relate the optimal N to the maximum NFG response, where local maxima are interpreted as indicators of characteristic source positions. Alternative approaches include spectral analysis of $log_{10}({B_n}^2)$ in which breakpoints in the spectrum define the truncation level (Elysseieva,

2004; Oruç, 2011), as well as multi-band harmonic evaluation (Aydin, 2007; Sindirgi et al., 2008) and hybrid criteria combining depth, maximum NFG, and error metrics (Zhang & Meng, 2015).

Following Alipour et al. (2023b), we adopt a robust adaptive procedure for determining N and resolving complex anomalous structures. First, an upper bound for N is estimated from the relationship between $log_{10}({B_{\mathrm{n}}}^2)$ and increasing harmonic numbers. NFG responses are then computed sequentially across harmonic levels up to this limit. At each spatial position, the maximum NFG value across all harmonics is extracted, and these maxima are subsequently integrated to construct the final NFG model.

As demonstrated in Alipour et al. (2023b), tracing maximum NFG responses across successive harmonic intervals provides a practical criterion for imaging and depth interpretation of complex gravity anomalies. The progressive behavior of NFG maxima across the harmonic spectrum offers a consistent framework for relating long- and short-wavelength gravity responses. Accordingly, this study adopts maximum-response tracing as the principal imaging criterion within the NFG workflow. When interpreted alongside the structural information derived from the UCRD framework, the resulting images become more coherent.

The performance of the proposed methodology is evaluated using three synthetic models presented in the following section. Since the theoretical basis and numerical implementation of the NFG method have been comprehensively established in previous studies, only those aspects required for the present application are considered here.

3. Synthetic tests

To evaluate the capability of the UCRD and NFG frameworks for structural reconstruction and depth characterization from gravity data, three synthetic models of increasing structural complexity were designed (Fig. 1). The models were selected to examine the performance of the proposed methodology under a range of scenarios, including isolated bodies, overlapping sources, and laterally extensive multi-level structures.

The first synthetic model (Fig. 1a; Table 1) consists of six cubic bodies with different dimensions, depths, and density contrasts, together with three stepped structures. This model provides a comprehensive benchmark for assessing the ability of the proposed methodology to resolve multiple isolated and adjacent sources exhibiting varying geometries and amplitudes. Similar configurations have been widely employed for evaluating the stability, resolution, and reliability of gravity interpretation methods (Oldenburg, 1974; Li & Oldenburg, 1998; Williams, 2008; Rezaie et al., 2017; Vatankhah et al., 2018; Lin & Zhdanov, 2018; Zhao et al., 2018; Zhang et al., 2018; Fregoso et al., 2020).

The second synthetic model (Fig. 1b; Table 2) comprises two partially overlapping blocks together with a shallow cubic body. The overlapping sources generate a complex composite gravity response characterized by merged anomaly signatures and distorted peak geometries. This model was specifically designed to investigate the ability of the proposed framework to distinguish closely spaced sources and preserve structural continuity in the presence of overlapping gravitational effects.

The third synthetic model (Fig. 1c; Table 3) consists of a laterally extensive structure represented by twenty-five individual blocks distributed at different depths. Such configurations are particularly challenging because the resulting gravity anomaly is dominated by long-wavelength

responses and does not readily reveal the internal structural complexity of the causative bodies. Similar models have previously been used to evaluate gravity interpretation methodologies (Zhang & Wong, 2015; Zhang et al., 2018). Consequently, this model provides a rigorous test of the capability of UCRD to reconstruct large-scale structural geometry and of NFG to characterize depth variations within spatially extensive source systems.

3.1. Synthetic model 1

Figure 2 illustrates the application of the UCRD framework to Synthetic Model 1. The decomposition process generates seven restricted wavelength levels through successive upward continuation, with continuation heights (Δz) ranging from 0.6 to 242.1 km. At each level, the upward-continued field from the previous stage serves as the input for the subsequent decomposition step, producing a hierarchical representation of the gravity field across progressively increasing wavelength ranges. The resulting RWL are subsequently transformed into SRWL.

The decomposition reveals a systematic evolution of anomaly responses with increasing continuation height. Shallow components dominate the lower levels, whereas deeper and longer-wavelength contributions become increasingly prominent at larger Δz values. For Synthetic Model 1, the principal anomalous bodies are most clearly expressed between levels 3 and 6 (Δz = 4.4–89 km), indicating that these continuation intervals contain the dominant structural information associated with the model. Although the overall spatial patterns of the RWL and SRWL responses remain comparable, the SRWL transformation produces sharper and more localized anomaly signatures, thereby improving structural definition and enhancing the continuity of reconstructed features.

To evaluate the three-dimensional imaging capability of the proposed framework, Figure 3 presents vertical sections extracted along three XZ profiles (Y = 96, 300, and 504 km) and three YZ profiles (X = 96, 300, and 504 km). The UCRD sections were generated by interpolating between the seven SRWL levels shown in Figure 2d. Comparison with the true model geometry demonstrates that the reconstructed sections successfully recover the overall spatial distribution, polarity, and lateral extent of the synthetic bodies. While UCRD provides a continuous representation of subsurface structural geometry, it does not directly estimate source depth because the vertical axis corresponds to upward-continuation height rather than physical depth.

To constrain source depth, the UCRD results are integrated with NFG imaging. The corresponding NFG sections shown in Figure 3 provide quantitative depth information and exhibit strong spatial agreement with the reconstructed UCRD structures. Consequently, the two methods provide complementary information: UCRD delineates the geometry and polarity of subsurface structures, whereas NFG supplies independent depth constraints.

Following the imaging criterion proposed by Alipour et al. (2023b), maximum NFG responses were traced across increasing harmonic intervals to identify the optimal harmonic number (N). Figure 4 illustrates the procedure for the profile at Y = 96 km. The logarithmic harmonic-energy spectrum (Fig. 4b) exhibits a transition zone between long-wavelength and short-wavelength regimes, indicating the range within which the optimal harmonic solution is expected to occur. For this profile, the transition is centered near $N \approx 29$. The corresponding NFG responses for N = 27–31 (Fig. 4a) demonstrates progressive focusing of anomaly maxima, with the most coherent and spatially concentrated responses occurring at N = 28 and N = 29. These solutions provide the most reliable depth estimates and exhibit the strongest agreement with the known geometry of the synthetic model.

3.2. Synthetic model 2

Figure 5 illustrates the application of the UCRD framework to Synthetic Model 2 (Fig. 1b; Table 2). The decomposition process generates seven restricted wavelength levels with continuation heights (Δz) ranging from 0.6 to 242.1 km. At each level, the gravity field is progressively separated into wavelength-restricted components, which are subsequently transformed into SRWL representations. Comparison between the RWL and SRWL responses demonstrates that the normalization procedure significantly improves structural definition. In particular, the SRWL levels provide sharper and more localized anomaly responses, allowing clearer discrimination between the shallow cube and the deeper overlapping bodies. This improvement is most evident between levels 4 and 6, where the structural transition from shallow to deep sources becomes more clearly resolved.

The reconstructed geometry is further examined through vertical sections extracted along the XZ profile at Y = 250 km and the YZ profile at X = 250 km (Fig. 6). As in Synthetic Model 1, the UCRD sections successfully recover the overall geometry of the causative structures despite the complexity introduced by overlapping sources. The overlapping blocks generate composite anomaly responses that are difficult to interpret directly from the gravity field alone; however, the UCRD reconstruction separates the dominant structural components and provides a coherent representation of their spatial relationships. The corresponding NFG sections supply quantitative depth information and exhibit strong agreement with the reconstructed geometry.

The NFG imaging criterion based on tracing maximum responses across increasing harmonic intervals is illustrated in Figure 7 for the profile at Y = 250 km. The harmonic-energy spectrum indicates a transition from long-wavelength to short-wavelength responses near N = 11,

corresponding to the dominant deep structure. Examination of the NFG responses shows progressive focusing of anomaly maxima between N = 11 and N = 13, followed by a rapid transition at N = 14. Because the responses at N = 11–13 are highly consistent, N = 11 was selected as the most stable representative harmonic number for the long-wavelength component and was subsequently used for depth characterization in Figure 6.

An additional short-wavelength feature is evident in the UCRD reconstruction, producing an asymmetric geometry associated with the shallow body located near X = 100 km (Fig. 6a). This feature is independently supported by a stable NFG response at N = 39, which delineates the left boundary of the shallow structure immediately before the onset of artifact responses. The agreement between the UCRD reconstruction and the corresponding NFG solution demonstrates the ability of the combined framework to distinguish overlapping sources and to characterize both shallow and deep structural components within a single gravity dataset.

3.3. Synthetic model 3

Figure 8 illustrates the application of the UCRD framework to Synthetic Model 3 (Fig. 1c; Table 3). The decomposition generates seven restricted wavelength levels with continuation heights (Δz) ranging from 0.6 to 242.1 km. As in the previous examples, the gravity field is progressively separated into wavelength-restricted components and subsequently transformed into SRWL representations. Comparison of the RWL and SRWL responses demonstrates the effectiveness of the scaling procedure in enhancing structural expression. The improvement is particularly evident between levels 3 and 5, where the SRWL responses exhibit sharper and more localized anomaly patterns. For example, the shallow blocks located at depths of 10–20 km are clearly expressed in the level-4 SRWL response, whereas their signatures are substantially less distinct in the

corresponding RWL representation. These results indicate that the SRWL transformation improves the resolution of both shallow and intermediate-depth structural components within laterally extensive source systems.

Figure 9 presents vertical sections of the gravity anomaly, UCRD reconstruction, and NFG responses along XZ profiles at Y = 50 km and Y = 100 km and YZ profiles at X = 50 km and X = 100 km. Despite the complexity of the model and the large number of individual source bodies, the UCRD reconstruction successfully recovers the overall geometry of the composite structure. The reconstructed sections reveal both shallow and deep structural components, demonstrating the capability of the method to image source distributions that are difficult to recognize directly from the gravity anomaly alone. The corresponding NFG sections provide complementary depth information and exhibit good agreement with the reconstructed geometry.

The NFG imaging criterion based on tracing maximum responses across increasing harmonic intervals is illustrated in Figure 10 for the profile at Y = 100 km. The harmonic-energy spectrum indicates a characteristic transition near N = 21, corresponding to the dominant component of the model. Harmonic numbers N = 12–14 produce focused maxima associated with the deeper structures, whereas harmonic numbers N = 20–22 emphasize the extended shallow to deep components. The presence of these two stable harmonic regimes demonstrates the ability of the combined UCRD–NFG framework to resolve multiple depth levels within complex and laterally extensive gravity-source configurations.

4. Discussion on synthetic tests

The synthetic experiments demonstrate the complementary roles of the UCRD and NFG frameworks for gravity interpretation. UCRD provides a interpretable reconstruction of subsurface structural geometry by decomposing the gravity field into RWL components and enhancing their structural expression through the SRWL transformation. In contrast, NFG supplies quantitative depth information through analysis of harmonic-domain gradient responses. Used together, the two methods enable simultaneous characterization of structural geometry and source depth from gravity data alone.

A particular advantage of the combined framework is its ability to reduce ambiguities associated with NFG interpretation. Previous studies have shown that tracing maximum NFG responses across increasing harmonic intervals provides an effective imaging criterion for identifying source depths and selecting the optimal harmonic number (Alipour et al., 2023b). However, NFG responses may be difficult to interpret in complex situations because anomaly maxima can originate from source boundaries, internal structural variations, or overlapping responses from bodies located at different depths. Furthermore, identification of the appropriate harmonic number is not always straightforward. In such cases, the geometric information provided by UCRD serves as an independent constraint, facilitating discrimination between competing NFG solutions and improving confidence in the interpretation.

An additional advantage of the proposed methodology is that it operates directly on gravity data and does not require supplementary geophysical information or a priori structural constraints. Consequently, preliminary structural characterization can be performed without reliance on seismic data (Zhdanov, 2002; Farquharson & Oldenburg, 2004; Bosch et al., 2010; Moorkamp et al., 2011), computationally intensive inversion procedures (Oldenburg, 1974; Li & Oldenburg, 1998; Zhao et al., 2018; Zhang et al., 2018), joint inversion strategies (Gallardo & Meju, 2004;

Lelièvre et al., 2012; Lin & Zhdanov, 2018; Ming et al., 2024), or forward modelling approaches (Talwani & Ewing, 1960; Nagy, 1966). Although UCRD is not intended to replace these methodologies, the reconstructed structural geometries can provide valuable starting models, geometric constraints, and parameterization guidance for subsequent forward modelling and inversion studies.

The three synthetic models were designed to evaluate the performance of the proposed framework under progressively more challenging conditions. Synthetic Model 1 assessed the capability of the method to reconstruct multiple isolated and adjacent bodies with varying dimensions and density contrasts. Synthetic Model 2 examined the ability of the framework to resolve overlapping sources and distinguish shallow from deeper structural components. Synthetic Model 3 provided a rigorous test of large-scale structural reconstruction in a laterally extensive multi-level system characterized by substantial depth variability. Across all three experiments, the UCRD reconstructions showed good agreement with the true model geometries, while the NFG responses provided consistent depth estimates. The results demonstrate that the combined UCRD–NFG framework is capable of recovering both structural geometry and depth characteristics over a broad range of source configurations and complexity levels.

Synthetic model 1. The UCRD results for Synthetic Model 1 are presented in Figure 2d, where the horizontal SRWL levels constitute the primary output of the decomposition procedure. The vertical sections shown in Figure 3 are generated by interpolation between the seven SRWL levels. Although the interpolation process smooths some fine-scale features, the resulting sections provide a useful representation of the reconstructed geometry and allow direct comparison with the corresponding NFG depth responses.

The first prominent UCRD responses appear at level 3 and correspond to stepped blocks 1–3 together with the shallow positive-density cubes. According to Table 1, these bodies begin at depths of approximately 10 km and possess positive density contrasts. Their responses remain visible through levels 4 and 5 before gradually diminishing at higher continuation levels. Particularly strong positive anomalies are observed in Figure 3a (XZ profile at (500, 96) km), Figure 3b (XZ profile at (300, 300) km), and Figure 3c (XZ profile at (100, 504) km). In all cases, increasing continuation height is associated with increasing source depth, and corresponding NFG maxima occur at harmonic numbers N = 28, N = 31, and N = 35, respectively.

The response of stepped block 1 is especially evident in Figure 3a. The NFG maximum at N = 28 delineates the lower portion of the structure, highlighted by the red interior circle. At this location, the response of stepped block 1 is influenced by the adjacent shallow cube, producing a composite anomaly pattern. Examination from an alternative viewing direction (YZ profile at (504, 100) km) in Figure 3f reveals a sharp UCRD response together with a stable NFG maximum at N = 60. Combining the UCRD reconstruction, NFG responses, and the SRWL levels shown in Figure 2d indicates the presence of a large stepped structure that extends from near-surface depths to greater than 50 km. This geometry is particularly evident in Figure 3f, where the UCRD response begins at shallow depth near Y ≈ 10 km, reaches depths of approximately 50 km near Y ≈ 100 km, and then rises again toward shallower levels. The corresponding NFG maxima, marked by red circles, appear to delineate the structural boundaries of the body.

Similar behavior is observed for stepped block 2 and the adjacent shallow cube near coordinates YZ profile at (96, 500) km in Figure 3d. For stepped block 2, in Figure 3c (XZ profile at (100, 504) km), the UCRD reconstruction and the NFG response at N = 35 show excellent agreement with the known geometry of the synthetic model. Figure 3d further confirms this interpretation

460 through a stable NFG response at N = 57. Stepped block 3 (300, 300) km is clearly identified in
461 Figure 3b and Figure 3e, where both UCRD and NFG indicate a structure extending from near-
462 surface depths around Y = 250 km to depths exceeding 50 km near Y = 350 km.

463 The six cubic bodies provide an additional test of the ability of the proposed framework to resolve
464 structures with different geometries, depths, and density contrasts. Cube 1 ((300, 500) km) is
465 recovered particularly well, as demonstrated by the strong agreement between the UCRD
466 reconstruction and NFG responses in Figure 3c (N = 54) and Figure 3e (N = 104). Cube 3 ((100,
467 300) km) is also successfully recovered in Figure 3d (N = 43) and Figure 3b (N = 67), while cube
468 5 ((100, 100) km) produces clear UCRD responses and NFG maxima at N = 29 and N = 38. The
469 N = 29 response corresponds approximately to the center of the body, whereas N = 38 is more
470 closely associated with its upper boundary. The cube 6 (300, 100) km is represented in Figure 3a
471 (N = 28) and Figure 3e (N = 33), providing a reasonable reconstruction of its geometry and depth.

472 The deepest bodies in the model, cubes 2 (500, 500) km and 4 (500, 300) km, present a greater
473 challenge because their responses are partially masked by shallower structures. Consequently,
474 UCRD occasionally places these bodies at shallower apparent depths, and NFG responses may be
475 weak or absent in some profiles. For example, cube 4 produces only a weak NFG response in
476 Figure 3b at N = 29, while cube 2 is represented by a response at N = 20 in Figure 3c. In Figure
477 3f, cube 4 is associated with N = 32, whereas cube 2 does not produce a clearly identifiable NFG
478 maximum. Although some profiles underestimate depth, alternative viewing directions generally
479 recover the correct structural position. This behavior is consistent with previous studies
480 demonstrating that deep sources can be partially obscured by dominant shallow anomalies (e.g.,
481 Rezaie et al., 2017).

The performance of the proposed framework compares favorably with previously published investigations of this benchmark model, including studies by Zhang and Wong (2015), Lin and Zhdanov (2018), Vatankhah et al. (2018), Fregoso et al. (2020), and Yang et al. (2020). These studies show that unconstrained inversion often struggles to recover the true geometry of complex source distributions and generally requires additional constraints, depth weighting, or complementary geophysical information. In contrast, UCRD provides a direct representation of structural geometry from gravity data alone, while NFG independently supplies depth information. The combination of the two approaches therefore offers a practical means of reconstructing both geometry and depth prior to more computationally intensive inversion procedures. As noted by Williams (2008), Synthetic test similar to Model 1 represents a particularly demanding test because it contains bodies with different geometries, density contrasts, polarities, and burial depths. Nevertheless, the strongest UCRD and NFG responses consistently correspond to the principal structural elements of the model, demonstrating the effectiveness of the proposed methodology under complex multi-source conditions.

Synthetic model 2. Synthetic Model 2 (Fig. 1b; Table 2) consists of three rectangular prisms: a shallow, relatively small prism (Prism 1), an intermediate-depth prism (Prism 2), and a deeper prism (Prism 3). The partial overlap between Prisms 2 and 3 produces a high-density overlap zone, generating a complex gravity response that makes structural recovery particularly challenging.

The UCRD decomposition results (Fig. 5d) reveal the progressive emergence of the different source bodies with increasing continuation height. Prism 1, located near coordinates (100, 250), is primarily expressed at levels 3 and 4, whereas Prism 2, centered near (250, 150), becomes most apparent at levels 4 and 5. The strongest responses associated with the overlapping deeper prisms occur at level 6. These observations indicate that the UCRD decomposition successfully separates

505 the shallow and deep structural contributions despite the significant interference produced by the
506 overlap zone.

507 The reconstructed geometry is further illustrated in the vertical sections of Figure 6. In Figure 6a,
508 the shallow body near (100, 250) km is identified within the UCRD reconstruction as
509 unsymmetrical edge and is associated with a stable NFG response at N = 39. The NFG maximum
510 occurs along the outer boundary of the structure and provides a reliable depth estimate for the
511 shallow prism. The central overlapping region near (250, 250) exhibits particularly good
512 agreement between the UCRD reconstruction and the true model geometry. In this area, the upward
513 continuation height correlates closely with the actual depth distribution of the source bodies, while
514 the NFG responses provide independent quantitative depth constraints.

515 The YZ section shown in Figure 6b further demonstrates the capability of the combined UCRD–
516 NFG framework. Although the UCRD reconstruction slightly overestimates depth in parts of the
517 section, the corresponding NFG responses at N = 12 and N = 14 delineate the depth extent of the
518 structure through its lateral boundaries. The complementary nature of the two methods is
519 particularly evident in this profile: UCRD provides the overall structural geometry, whereas NFG
520 supplies more precise depth information where the geometry alone becomes ambiguous.

521 This synthetic model represents a demanding test because the overlapping prisms generate
522 composite anomaly signatures that obscure the true source geometry. Nevertheless, the combined
523 interpretation of Figures 5 and 6 demonstrates that UCRD and NFG together provide detailed
524 information on both structural configuration and depth distribution. Similar difficulties have been
525 reported in previous studies of gravity inversion. As illustrated by the response in Figure 6b, NFG
526 recovery becomes increasingly challenging for laterally extensive bodies, where maxima are often
527 concentrated near structural boundaries rather than within the interior of the source. Comparable

challenges have been discussed by Zhang and Wong (2015) in the recovery of horizontally extensive bodies and by Sun et al. (2021) in three-dimensional gravity inversion on unstructured grids. The present results indicate that the integration of UCRD and NFG provides a practical means of addressing such ambiguities by combining geometric reconstruction with independent depth estimation.

Synthetic model 3. Synthetic Model 3 (Fig. 1c; Table 3) represents a laterally extensive structure composed of multiple blocks distributed at different depths. The UCRD decomposition results (Fig. 8d) exhibit well-defined responses between levels 3 and 5, corresponding to the progression from the shallowest to the deepest structural components of the model. Comparison with the true geometry (Fig. 1c) indicates that these levels contain the principal information associated with the reconstructed structure.

To examine the three-dimensional geometry of the model, four vertical profiles were analyzed (Fig. 9). The UCRD sections (Figs. 9a–d) consistently reveal a broad anomalous body extending approximately from X = 50 to 150 km and from Y = 50 to 150 km. This continuity suggests the presence of a laterally extensive structure with relatively uniform density characteristics. The corresponding NFG responses provide additional depth constraints and reveal variations that are not immediately apparent from the UCRD reconstruction alone.

For the XZ profile at Y = 50 km (Fig. 9a), the NFG response at N = 21 identifies a shallow structural boundary at depths of approximately 10–20 km. Along the YZ profile at X = 50 km (Fig. 9c), a deeper edge response is observed at depths of approximately 15–25 km, also corresponding to N = 21. In addition, a weaker NFG maximum occurs near coordinates (50, 100) at N = 29, which is interpreted as a deeper block located at approximately 20–30 km depth.

The profile at Y = 100 km (Fig. 9b) reveals a bowl-shaped structure extending from approximately 10 to 30 km depth. The principal response is associated with N = 21, while two edge-related maxima occur at N = 13 and correspond to depths of approximately 20–30 km. Similarly, the YZ profile at X = 100 km (Fig. 9d) exhibits an edge response at N = 16 associated with depths of approximately 20–30 km, together with a weaker response at N = 21 corresponding to the shallower portion of the structure.

The combined interpretation of the UCRD decomposition (Fig. 8d) and the NFG depth responses (Fig. 9) indicates that the model is characterized by a laterally continuous body extending across much of the central part of the study area. The UCRD results define the overall geometry and spatial continuity of the structure, whereas the NFG responses identify distinct depth levels and structural boundaries. Together, the results suggest a relatively uniform-density body extending from approximately 10 to 30 km depth, in excellent agreement with the geometry of the synthetic model.

5. Conclusions

This study introduced the Upward Continuation Restriction to Decomposition (UCRD) method, a spectral framework designed to reconstruct subsurface structural geometry directly from Bouguer gravity anomalies. Through successive upward continuation and restricted-wavelength decomposition, the gravity field is separated into a series of depth-related components that progressively reveal the spatial organization of subsurface density contrasts. Application of a three-dimensional analytic signal transformation followed by scale-adaptive normalization produces scaled restricted wavelength (SRWL) responses that preserve anomaly polarity, retain physical

572 units (mGal), and provide a physically interpretable representation of subsurface structural
573 geometry.

574 Because gravity anomalies alone do not uniquely constrain source depth, UCRD was integrated
575 with the normalized full gradient (NFG) method. Within this framework, UCRD provides
576 geometric characterization of subsurface structures, whereas NFG supplies independent depth
577 constraints through harmonic-domain gradient analysis. The combined methodology therefore
578 enables simultaneous interpretation of structural geometry and source depth using gravity data
579 alone.

580 Evaluation using three synthetic models representing isolated bodies, overlapping structures, and
581 laterally extensive multi-level sources demonstrates that the proposed framework is capable of
582 recovering both horizontal and vertical structural patterns over a broad range of source
583 configurations. The SRWL responses consistently provide sharper and more localized structural
584 signatures than the original gravity anomalies and conventional restricted-wavelength
585 components, improving the delineation of subsurface features. In parallel, NFG depth estimates
586 show strong agreement with the true source geometry and remain effective even in challenging
587 situations involving overlapping bodies, strong geometric contrasts, and laterally extensive
588 structures.

589 An important advantage of the proposed methodology is that it operates directly on gravity data
590 without requiring prior geological information, structural constraints, forward modelling, or
591 computationally intensive inversion procedures. Consequently, the UCRD–NFG framework can
592 serve as a rapid and computationally efficient interpretation tool, while also providing valuable
593 initial models and geometric constraints for subsequent inversion and integrated geophysical
594 investigations.

Although the method remains subject to limitations inherent to spectral decomposition, including partial wavelength overlap between adjacent levels and smoothing effects associated with vertical interpolation, the results demonstrate that UCRD provides a robust and intuitive approach for structural imaging from gravity data. The combined UCRD–NFG framework therefore represents a practical addition to the toolbox of gravity interpretation methods, particularly for regional-scale investigations where rapid characterization of subsurface geometry and depth is required.

Data availability statement

The synthetic datasets generated during this study and the MATLAB codes used for the UCRD and NFG analyses are available from the corresponding author upon reasonable request.

Authors contribution

Ako Alipour conceptualized the study, developed the algorithm, implemented the method, conducted the formal analysis, and drafted the manuscript. Khalil Motaghi conceptualized the study, supervised the research, and contributed to the method application. Zahra Mousavi supervised the project, assisted with method implementation and algorithm development.

Specific Tasks by Author:

Conceptualization: Ako Alipour, Khalil Motaghi, Zahra Mousavi

Method Implementation and Application: Ako Alipour, Khalil Motaghi, Zahra Mousavi

Results Interpretation: Ako Alipour, Khalil Motaghi, Zahra Mousavi

Data analysis: Ako Alipour, Khalil Motaghi

Discussion: Ako Alipour, Khalil Motaghi

Manuscript Drafting and Writing: Ako Alipour

Conflict of interest

The corresponding author states that there is no conflict of interest.

References

Aghajani, H., Moradzadeh, A. & Zeng, H.L., 2009a. Estimation of depth to salt domes from normalized full gradient of gravity anomaly and examples from the USA and Denmark. *Journal of Earth Science*, 20, 1012–1016. https://doi.org/10.1007/s12583-009-0088-y

Aghajani, H., Moradzadeh, A. & Zeng, H.L., 2009b. Normalized full gradient of gravity anomaly method and its application to the Mobrun Sulfide body, Canada. *World Applied Sciences Journal*, 6(3), 393–400.

Aghajani, H., Moradzadeh, A. & Zeng, H.L., 2011. Detection of high-potential oil and gas fields using normalized full gradient of gravity anomalies: A case study in the Tabas Basin, Eastern Iran. *Pure and Applied Geophysics*, 168, 1851–1863. https://doi.org/10.1007/s00024-010-0169-y

Agocs, W. B., 1951. Least-squares residual anomaly determination. *Geophysics*, 16(4), 686–696. https://doi.org/10.1190/1.1437720

Alipour, A., Motaghi, Kh. & Mousavi, Z., 2023a. Normalized Full Gradient Study of Bouguer Gravity Anomaly Profile of NorthWestern Iran. *Journal of the Earth and Space Physics*, 49(2), 407–421. http://doi.org/10.22059/jesphys.2023.349077.1007458

Alipour, A., Motaghi, K., Mousavi, Z., Cheraghi, H. & Saadat, S.A., 2023b. Adopting normalized full gradient method for regional-scale gravity modelling: a case study for Northwestern Iran. *Geophysical Prospecting*, 1–24. https://doi.org/10.1111/1365-2478.13433

Alipour, A., Motaghi, K., Mousavi, Z. & Scarponiet, M., 2025. A novel algorithm for 3D multi-level gravity interpretation: application to northwestern Iran. Research Square Preprint, Version 1. https://doi.org/10.21203/rs.3.rs-7401211/v1

Aydın, A., 1997a. Evaluation of Gravity Data in Terms of Hydrocarbon by Normalized Full Gradient, Variation and Statistic Methods, Model Studies and Application in Hasankale-Horasan Basin (Erzurum). Ph.D. Thesis, Karadeniz Technical University, Trabzon, Turkey.

Aydin, A., 2007. Interpretation of gravity anomalies with the normalized full gradient (NFG) method and an example. *Pure and Applied Geophysics*, 164, 2329–2344. https://doi.org/10.1007/s00024-007-0271-y

Balmino, G., Perosanz, F., Rummel, R., Sneeuw, N. & Sünkel, H., 1999. CHAMP, GRACE and GOCE: Mission concepts and simulations. *Bollettino Di Geofisica Teorica Ed Applicata*, 40, 309–319.

Berezkin, V.M., 1967. Application of the total vertical gradient of gravity for determination of the depth to the sources of gravity anomalies. *Razvedochnaya Geofizika (Exploration Geophysics)*, 18, 69–79.

Berezkin, V.M., 1973. Application of gravity exploration to reconnaissance of oil and gas reservoirs. Moscow: Nedra Publishing House (in Russian).

Berezkin, V.M., 1988. Method of the Total Gradient in Geophysical Prospecting. Moscow: Nedra (in Russian).

Berezkin, V.M. & Buketov, A.P., 1965. Application of the harmonic analysis for the interpretation of gravity data. *Prikladnaya Geofizika (Applied Geophysics)*, 46, 161–166 (in Russian).

Blakely, R. J., 1995. Potential Theory in Gravity and Magnetic Applications. Cambridge University Press.

Bosch, M., Mukerji, T. & Gonzalez, E. F., 2010. Seismic inversion for reservoir properties combining statistical rock physics and geostatistics: A review. *Geophysics*, 75(5), 75A165-75A176. https://doi.org/10.1190/1.3478209

Bracewell, R., 1984. The Fourier Transform and Its Applications. McGraw-Hill Book Co., New York.

Ciancara, B. & Marcak, H., 1979. Geophysical anomaly interpretation of potential fields by means of singular points method and filtering. *Geophysical Prospecting*, 27, 251–260.

664 Debeglia, N. & Corpel, J., 1997. Automatic 3-D interpretation of potential-field data using analytic signal
665 derivatives. *Geophysics*, 62(1), 87–96. https://doi.org/10.1190/1.1444149

666 Dondurur, D., 2005. Depth estimates for slingram electromagnetic anomalies from dipping sheet-like
667 bodies by the normalized full gradient method. *Pure and Applied Geophysics*, 162, 2179–
668 2195. https://doi.org/10.1007/s00024-005-2711-x

669 Doo, W. B., Hsu, S. K., Tsai, C. H. & Huang, Y. S., 2009. Using analytic signal to determine
670 magnetization/density ratios of geological structures. *Geophysical Journal International*, 179(1), 112–
671 124. https://doi.org/10.1111/j.1365-246X.2009.04297.x

672 Elysseieva, I. S. & Berezkin, V. M., 1973. Errors of calculation of spectral density and their influence on
673 accuracy of gravity data interpretation. *Razvedochnaya Geofizika (Exploration Geophysics)*, 55, 15–22 (in
674 Russian).

675 Elysseieva, I.S., 2004. Determination of original parameters of potential function depending on the study
676 depth interval. *Geofizichesky Vestnik (Geophysical bulletin)*, 1, 19–22 (In Russian).

677 Elysseieva, I.S. & Pašteka, R., 2018. Review paper: Historical development of the total normalized gradient
678 method in profile gravity field interpretation. *Geophysical Prospecting*, 67, 188–
679 209. https://doi.org/10.1111/1365-2478.12704

680 Farquharson, C.G. & Oldenburg, D.W., 2004. A comparison of automatic techniques for estimating the
681 regularization parameter in non-linear inverse problems. *Geophysical Journal International*, 156(3), 411–
682 425. https://doi.org/10.1111/j.1365-246X.2004.02190.x

683 Fedi, M. & Quarta, T., 1998. Wavelet analysis for the regional-residual and local separation of potential
684 field anomalies. *Geophysical Prospecting*, 46(5), 507–525. https://doi.org/10.1046/j.1365-
685 2478.1998.00105.x

686 Florio, G., 2018. Mapping the depth to basement by iterative rescaling of gravity or magnetic data. *Journal*
687 *of Geophysical Research: Solid Earth*, 123. https://doi.org/10.1029/2018JB015667

688 Fregoso, E., Palafox, A. & Moreles, M.A., 2020. Initializing Cross-Gradients Joint Inversion of Gravity
689 and Magnetic Data with a Bayesian Surrogate Gravity Model. *Pure and Applied Geophysics*, 177, 1029–
690 1041. https://doi.org/10.1007/s00024-019-02334-w

691 Gallardo, L. A. & Meju, M. A., 2004. Joint two-dimensional DC resistivity and seismic travel time
692 inversion with cross-gradients constraints. *Journal of Geophysical Research: Solid Earth*,
693 109(B3). https://doi.org/10.1029/2003JB002716

694 Heath, P., 2018. Quantifying the differences between gravity reduction techniques. *Exploration*
695 *Geophysics*, 49(6), 735–743. https://doi.org/10.1071/EG17094

696 Henderson, R. G., 1970. On the validity of the use of the upward continuation integral for total magnetic
697 intensity data. *Geophysics*, 35, 916–919.

698 Henderson, R. G. & Zietz, I., 1949. The upward continuation of anomalies in total magnetic intensity
699 fields. *Geophysics*, 14, 517–534. http://dx.doi.org/10.1190/1.1437560

700 Hinze, W. J., Von Frese, R. R. B. & Saad, A. H., 2012. Gravity and Magnetic Exploration. Principles,
701 Practices, and Applications. Cambridge University Press, New York.

702 Ismail-Zadeh, A., Adamia, S., Chabukiani, A., Chelidze, T., Cloetingh, S., Floyd, M., Gorshkov, A.,
703 Gvishiani, A., Ismail-Zadeh, T., Kaban, M. K., Kadirov, F., Karapetyan, J., Kangarli, T., Kiria, J.,
704 Koulakov, I., Mosar, J., Mumladze, T., Müller, B., Sadradze, N., Safarov, R., Schilling, F. & Soloviev, A.,
705 2020. Geodynamics, seismicity, and seismic hazards of the Caucasus. *Earth-Science Reviews*, 207, 103222.
706 https://doi.org/10.1016/j.earscirev.2020.103222

707 Jacobsen, B. H., 1987. A case for upward continuation as a standard separation filter for potential-field
708 maps. *Geophysics*, 52(8), 1138–1148. https://doi.org/10.1190/1.1442378

709 Keating, P. & Pinet, N., 2011. Use of non-linear filtering for the regional–residual separation of potential
710 field data. *Journal of Applied Geophysics*, 73(4), 315–322. https://doi.org/10.1016/j.jappgeo.2011.02.002

711 Lelièvre, P.G., Farquharson, C.G. & Hurich, C.A., 2012. Joint inversion of seismic traveltimes and gravity
712 data on unstructured grids with application to mineral exploration. *Geophysics*, 77(1), K1–K15.
713 https://doi.org/10.1190/geo2011-0154.1

714 Li, Y. & Oldenburg, D.W., 1998. 3-D inversion of Gravity Data. *Geophysics*, 63, 109–
715 119. http://dx.doi.org/10.1190/1.1444302

716 Lin, W. & Zhdanov, M.S., 2018. Joint multinary inversion of gravity and magnetic data using Gramian
717 constraints. *Geophysical Journal International*, 215, 1540–1557. https://doi.org/10.1093/gji/ggy351

718 Meng, Q., Guo, L., Zhang, S., Lou, H., Li, R. & others, 2025. Deep Learning in Gravity Research: A
719 Review. *Journal of Earth Science*, 36(4), 1808–1819. https://doi.org/10.1007/s12583-023-1926-x

720 Ming, Y., Ma, G., Wang, T., Ma, B., Meng, Q. & Li, Z., 2024. Power-Type Structural Self-Constrained
721 Inversion Methods of Gravity and Magnetic Data. *Remote Sensing*, 16(4),
722 681. https://doi.org/10.3390/rs16040681

723 Moorkamp, M., Heincke, B., Jegen, M., Roberts, A. & Hobbs, R. W., 2011. A framework for 3-D joint
724 inversion of MT, gravity, and seismic refraction data. *Geophysical Journal International*, 184(1), 477–
725 493. https://doi.org/10.1111/j.1365-246X.2010.04856.x

726 Nabighian, M. N., 1972. The analytic signal of two-dimensional magnetic bodies with polygonal cross
727 section: its properties and use for automated anomaly interpretation. *Geophysics*, 37, 507–
728 517. https://doi.org/10.1190/1.1440276

729 Nabighian, M. N. et al., 2005a. Historical development of the gravity method in exploration. *Geophysics*,
730 70(6), 63ND–89ND. https://doi.org/10.1190/1.2133785

731 Nagy, D., 1966. The gravitational attraction of a right rectangular prism. *Geophysics*, 31(2), 362–
732 371. https://doi.org/10.1190/1.1439779

733 Nettleton, L. L., 1954. Regionals, residuals, and structures. *Geophysics*, 19, 10–
734 22. https://doi.org/10.1190/1.1437966

735 Oldenburg, D. W., 1974. The inversion and interpretation of gravity anomalies. *Geophysics*, 39(4), 526–
736 536. https://doi.org/10.1190/1.1440444

737 Oruç, B., 2011. Source Location and Depth Estimation Using Normalized Full Gradient of Magnetic
738 Anomalies. *Yerbilimleri*, 33(2), 177–192.

739 Pail, R., 2023. Space Gravity Missions: CHAMP, GRACE, GRACE-FO, and GOCE, Satellite Projects. In:
740 Sideris, M.G. (ed.) *Encyclopedia of Geodesy*. Springer, Cham. https://doi.org/10.1007/978-3-319-02370-
741 0_29-2

742 Pasteka, R., 2000. 2D semi-automated and environmental methods in gravimetry and magnetometry.
743 Department of Applied and Environmental Geophysics, Comenius University, Bratislava.

744 Prabhu, K. M. M., 2014. Window Functions and Their Applications in Signal Processing. CRC Press,
745 Taylor & Francis Group.

746 Ravat, D., 2007. Upward and downward continuation. In: Gubbins, D. & Herrero-Bervera, E.
747 (eds.) *Encyclopedia of Geomagnetism and Paleomagnetism*. Springer, pp. 974–976.

748 Rezaie, M., Moradzadeh, A. & Kalateh, A.N., 2017. Fast 3D inversion of gravity data using solution space
749 prior-conditioned Lanczos bidiagonalization. *Journal of Applied Geophysics*, 136, 42–
750 50. https://doi.org/10.1016/j.jappgeo.2016.10.019

751 Simpson, S. M., 1954. Least squares polynomial fitting to gravitational data and density plotting by digital
752 computers. *Geophysics*, 19(2), 255–269. https://doi.org/10.1190/1.1437990

753 Sindirgi, P., Pamukçu, O. & Özyalin, S., 2008. Application of normalized full gradient method to
754 self-potential (SP) data. *Pure and Applied Geophysics*, 165, 409–427. https://doi.org/10.1007/S00024-008-
755 0308-X

756 Spector, A. & Grant, F. S., 1970. Statistical models for interpreting aeromagnetic data. *Geophysics*, 35(2),
757 293–302. https://doi.org/10.1190/1.1440092

758 Sun, S., Yin, C. & Gao, X., 2021. 3D Gravity Inversion on Unstructured Grids. *Applied Sciences.* 11, 722.
759 https://doi.org/10.3390/app1102072

760 Talwani, M. & Ewing, M., 1960. Rapid computation of gravitational attraction of three-dimensional bodies
761 of arbitrary shape. *Geophysics*, 25(1), 203–225. https://doi.org/10.1190/1.1438687

762 Vatankhah, S., Renaut, R.A. & Ebrahimzadeh Ardestani, V., 2018. A fast algorithm for regularized focused
763 3D inversion of gravity data using randomized singular-value decomposition. *Geophysics*, 83(4),
764 G25-G34. https://doi.org/10.1190/geo2017-0386.1

765 Wang, Z. et al., 2025. Application of the three-dimensional normalized full gradient method for
766 multiple-object identification in gravity exploration: a case study of the Dachang tin-polymetallic ore
767 district. *Journal of Geophysics and Engineering*, 22(6), 1743–1753. https://doi.org/10.1093/jge/gxaf105

768 Williams, N.C., 2008. Geologically-constrained UBC–GIF gravity and magnetic inversions with examples
769 from the Agnew-Wiluna greenstone belt, Western Australia. Ph.D. Thesis, University of British Columbia.

770 Xu, Y., Hao, T., Li, Z., Duan, Q. & Zhang, L., 2009. Regional gravity anomaly separation using wavelet
771 transform and spectrum analysis. *Journal of Geophysics and Engineering*, 6(3), 279–
772 287. https://doi.org/10.1088/1742-2132/6/3/007

773 Xuan, S., Shen, C., Shen, W., Wang, J. & Li, J., 2018. Crustal structure of the South-Eastern Tibetan Plateau
774 from gravity data: new evidence for clockwise movement of the Chuan–Dian rhombic block. *Journal of*
775 *Asian Earth Sciences*. https://doi.org/10.1016/J.JSEAES.2018.03.018

776 Yang, J., Liu, S. & Hu, X. 2020. Inversion of high-amplitude magnetic total field anomaly: An application
777 to the Mengku iron-ore deposit, northwest *China. Scientific Reports*, 10(1), 11949.
778 https://doi.org/10.1038/s41598-020-68494-1

779 Zeng, H.L., Meng, X.H., Yao, C.L., Li, X.M., Lou, H., Guang, Z.N. & Li, Z.P. 2002. Detection of reservoirs
780 from normalized full gradient of gravity anomalies and its application to Shengli oil field, East
781 China. *Geophysics*, 67, 1138–1147. https://doi.org/10.1190/1.1500375

782 Zeng, X., Li, X., Su, J., Liu, D. & Zou, H., 2012. An adaptive iterative method for downward continuation
783 of potential field data from a horizontal plane. *Geophysics*, 78, 43–52. https://doi.org/10.1190/geo2012-
784 0404.1

785 Zhang, S. & Meng, X., 2015. Improved normalized full-gradient method and its application to the location
786 of source body. *Journal of Applied Geophysics*. https://doi.org/10.1016/j.jappgeo.2014.12.015

787 Zhang, Y. & Wong, Y.S., 2015. BTTB-based numerical schemes for three-dimensional gravity field
788 inversion. *Geophysical Journal International*, 203(1), 243–256. https://doi.org/10.1093/gji/ggv301

789 Zhang, Y., Wu, Y. & Yan, J. et al., 2018. 3D inversion of full gravity gradient tensor data in spherical
790 coordinate system using local north-oriented frame. *Earth, Planets and Space*, 70,
791 58. https://doi.org/10.1186/s40623-018-0825-5

792 Zhanakulova, K., Adebiyet, B., Orynbassarova, E., Yerzhankyzy, A., Kassymkanova, K. K.,
793 Abdykalykova, R. & Zakariya, M., 2025. Application of Machine Learning Methods for Gravity Anomaly
794 Prediction. *Geosciences*, 15(5), 175. https://doi.org/10.3390/geosciences15050175

795 Zhao, G., Chen, B., Chen, L., Liu, J. & Ren, Z., 2018. High-accuracy 3D Fourier forward modeling of
796 gravity field based on the Gauss-FFT technique. *Journal of Applied Geophysics*, 150, 294–
797 303. https://doi.org/10.1016/j.jappgeo.2018.01.002

Zhdanov, M. S., 2002. Geophysical Inverse Theory and Regularization Problems. Elsevier.

Figures

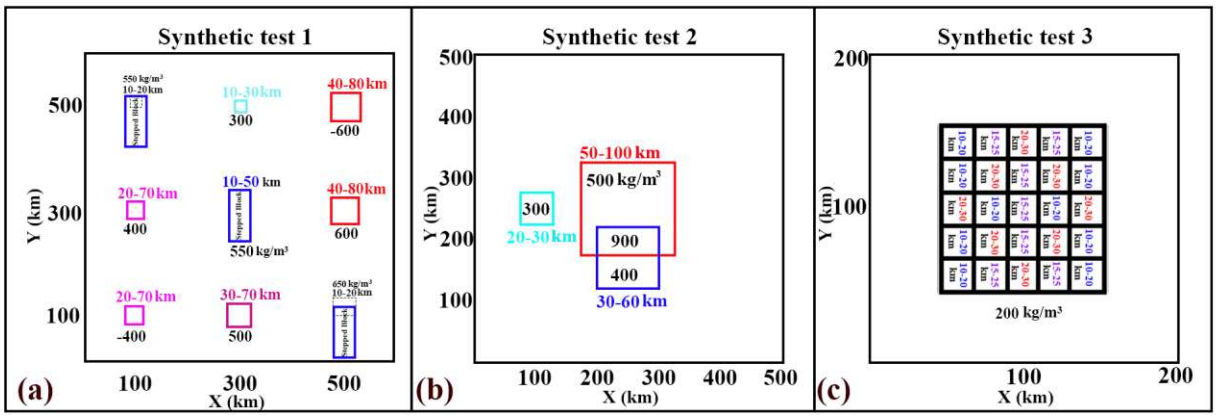


Figure 1. (a) Synthetic Model 1, (b) Synthetic Model 2 and (c) Synthetic Model 3.

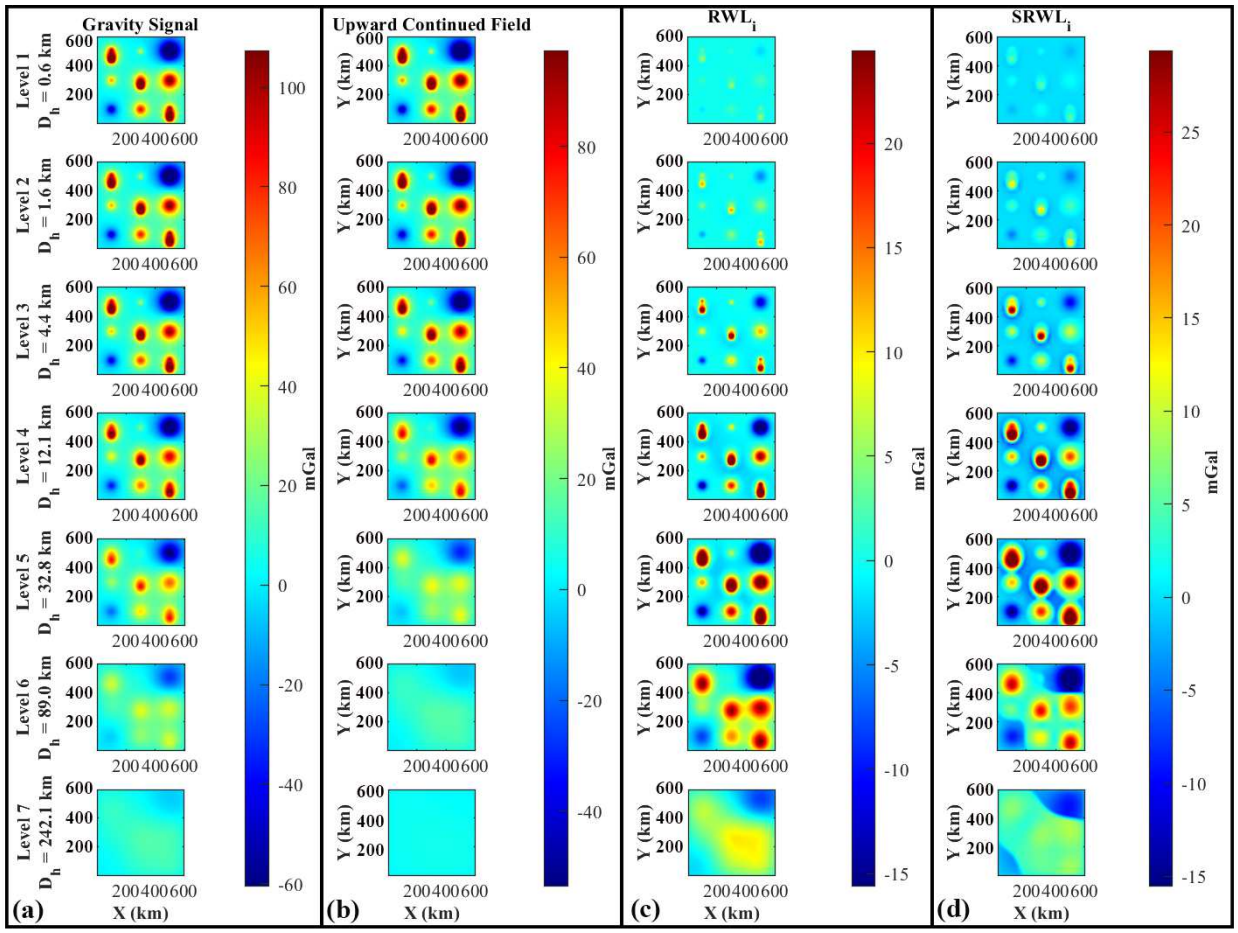


Figure 2. Step-by-step UCRD procedure for synthetic model 1 (Fig. 1a and Table 1). (a) Gravity signal, (b) upward continued field, (c) RWL_i, and (d) $SRWL_i$ at each UCRD level.

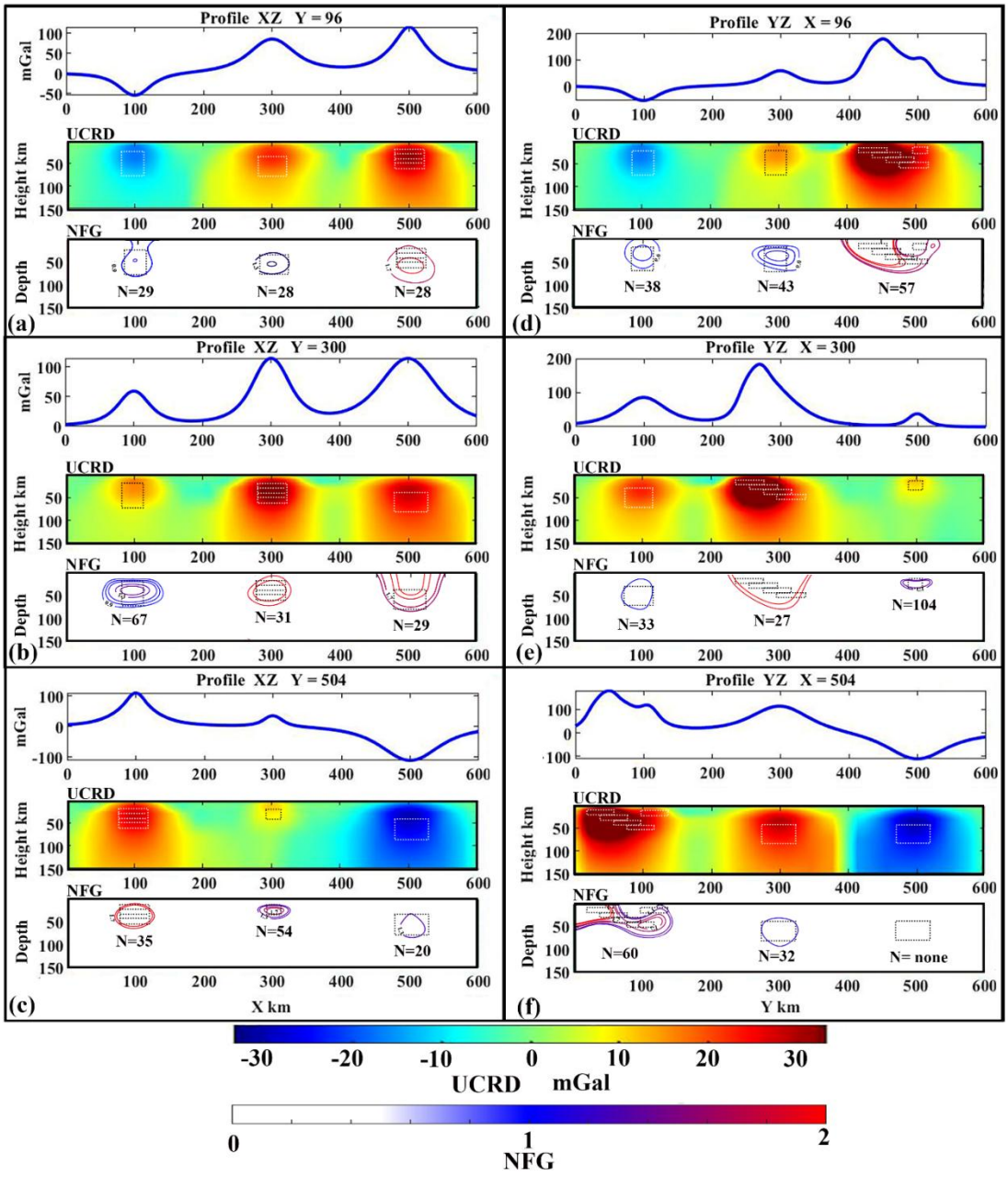


Figure 3. Vertical sections of the gravity anomaly, UCRD, and NFG responses for Synthetic Model 1 along XZ profiles at (a) Y = 96 km, (b) Y = 300 km, and (c) Y = 504 km, and along YZ profiles at (d) X = 96 km, (e) X = 300 km, and (f) X = 504 km. The true geometry of the synthetic bodies is outlined by dashed white rectangles in the UCRD panels and dashed black rectangles in the NFG panels. UCRD responses aredisplayed in mGal, whereas the corresponding NFG intensity scale is shown beneath the UCRD color bar.

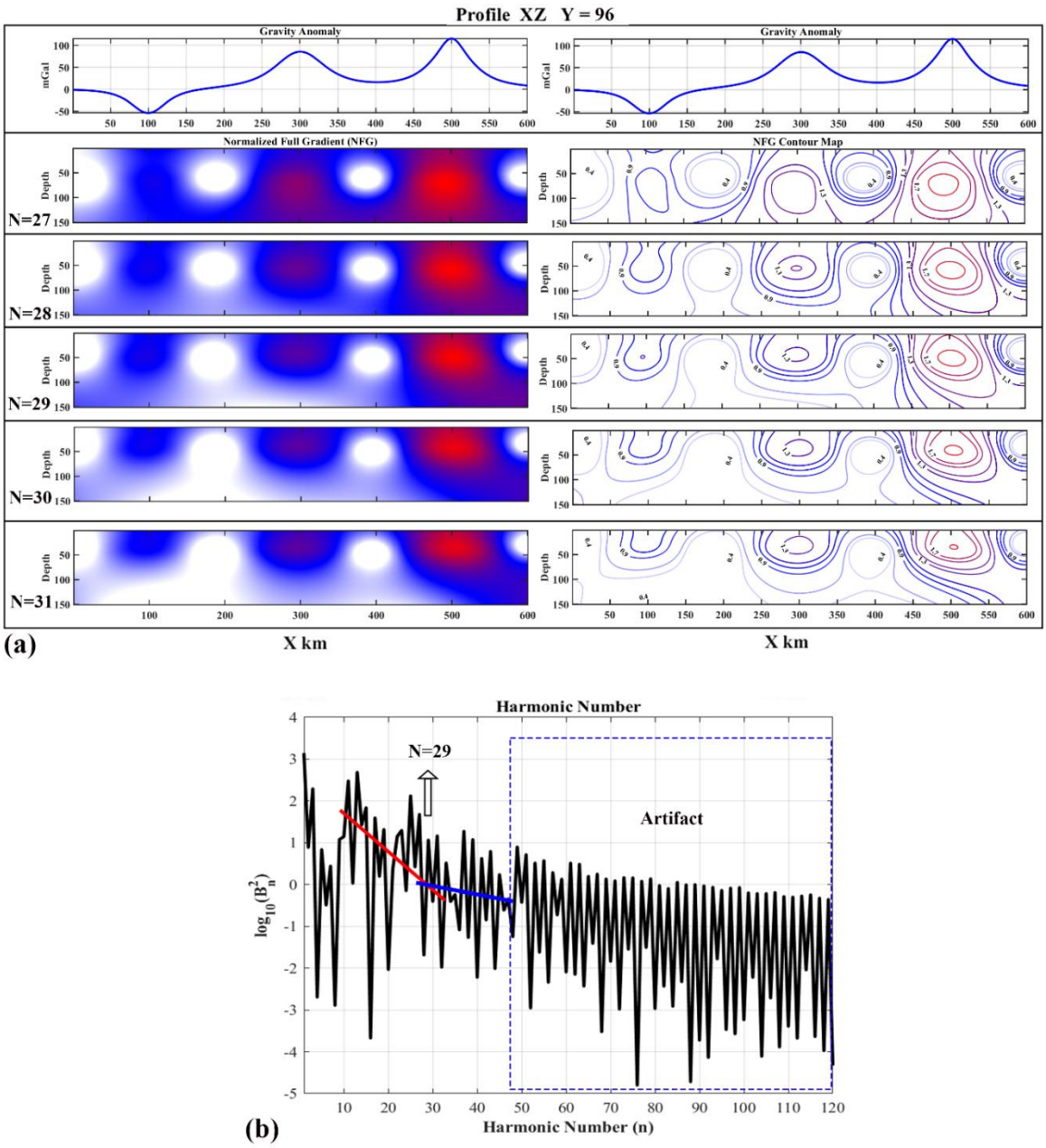
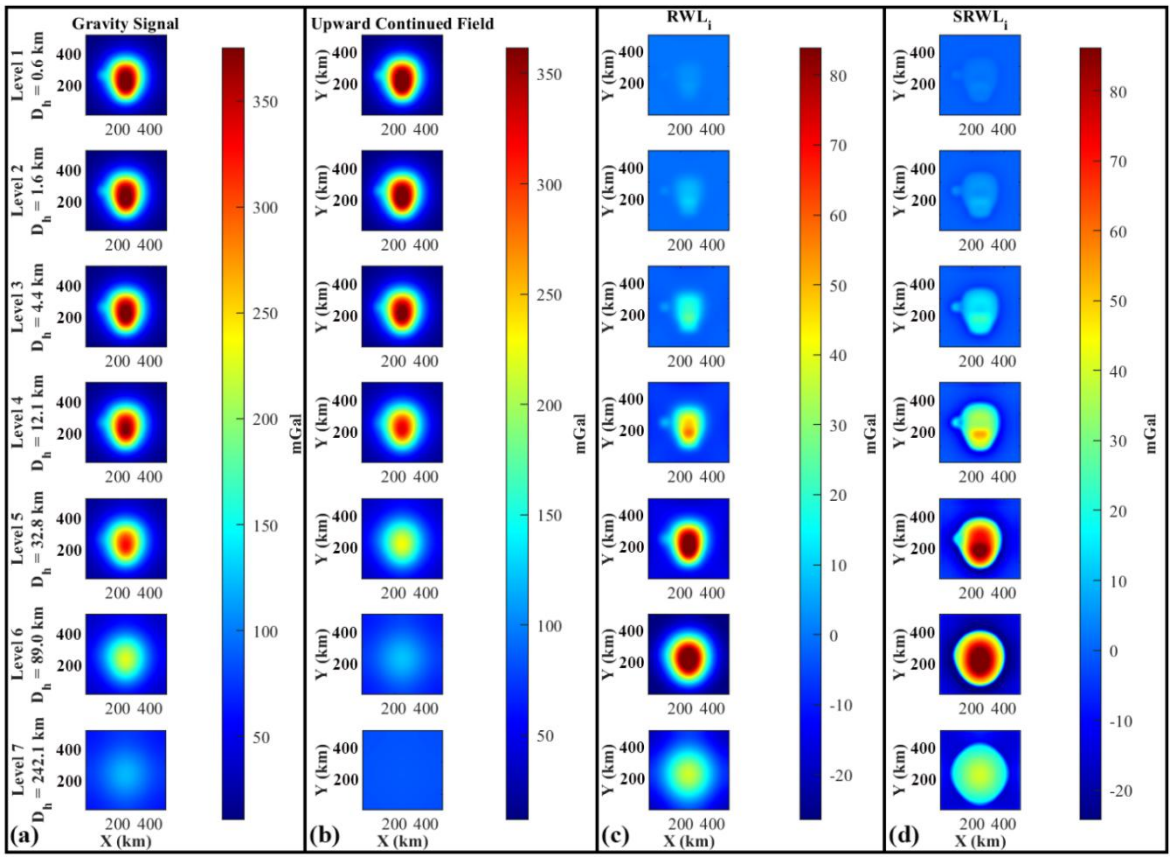


Figure 4. (a) NFG responses along the XZ profile at Y = 96 km for harmonic numbers n = 27–31. Color maps are shown on the left and corresponding contour maps on the right. (b) Harmonic-energy spectrum showing harmonic number n on the x-axis and $log_{10}(B_n{}^2)$ on the y-axis. The red and blue lines represent the low-degree (long-wavelength) and high-degree (short-wavelength) harmonic trends, respectively. The transition between these trends defines the optimal harmonic number (N = 29). The blue dashed rectangle denotes the artifact region, where harmonic responses are not considered interpretable.

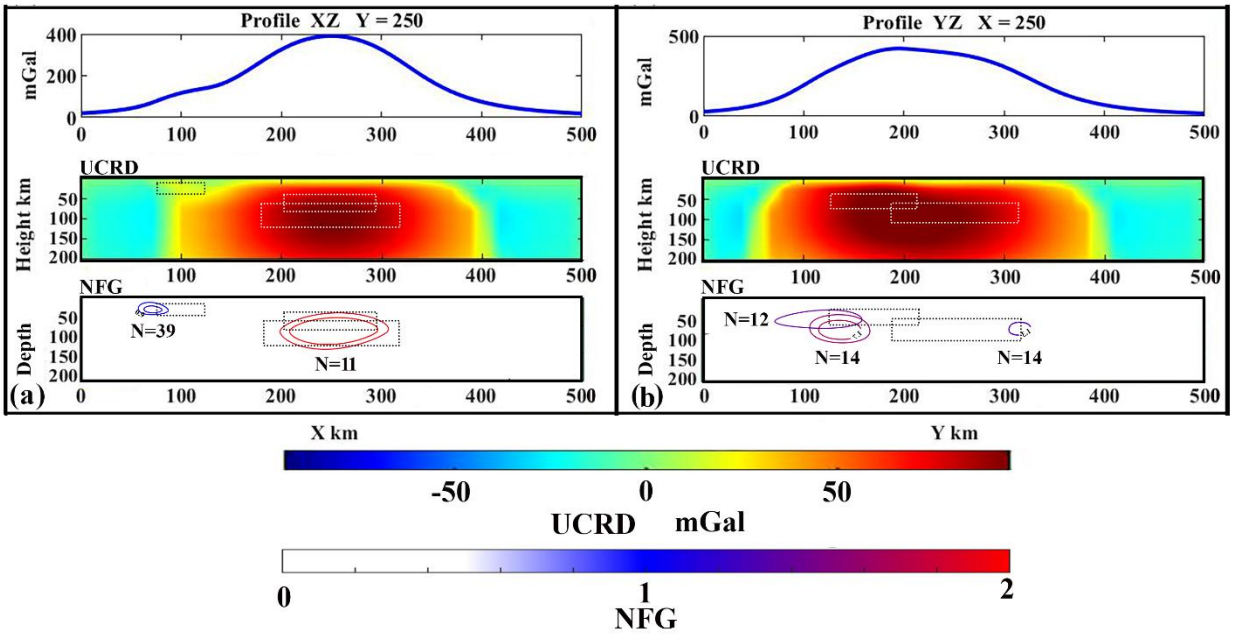
828



829 **Figure 5.** Step-by-step UCRD procedure for synthetic model 2 (Fig. 1b and Table 2). (a) Gravity signal,

830 (b) upward continued field, (c) RWL_i, and (d) $SRWL_i$ at each UCRD level.

831

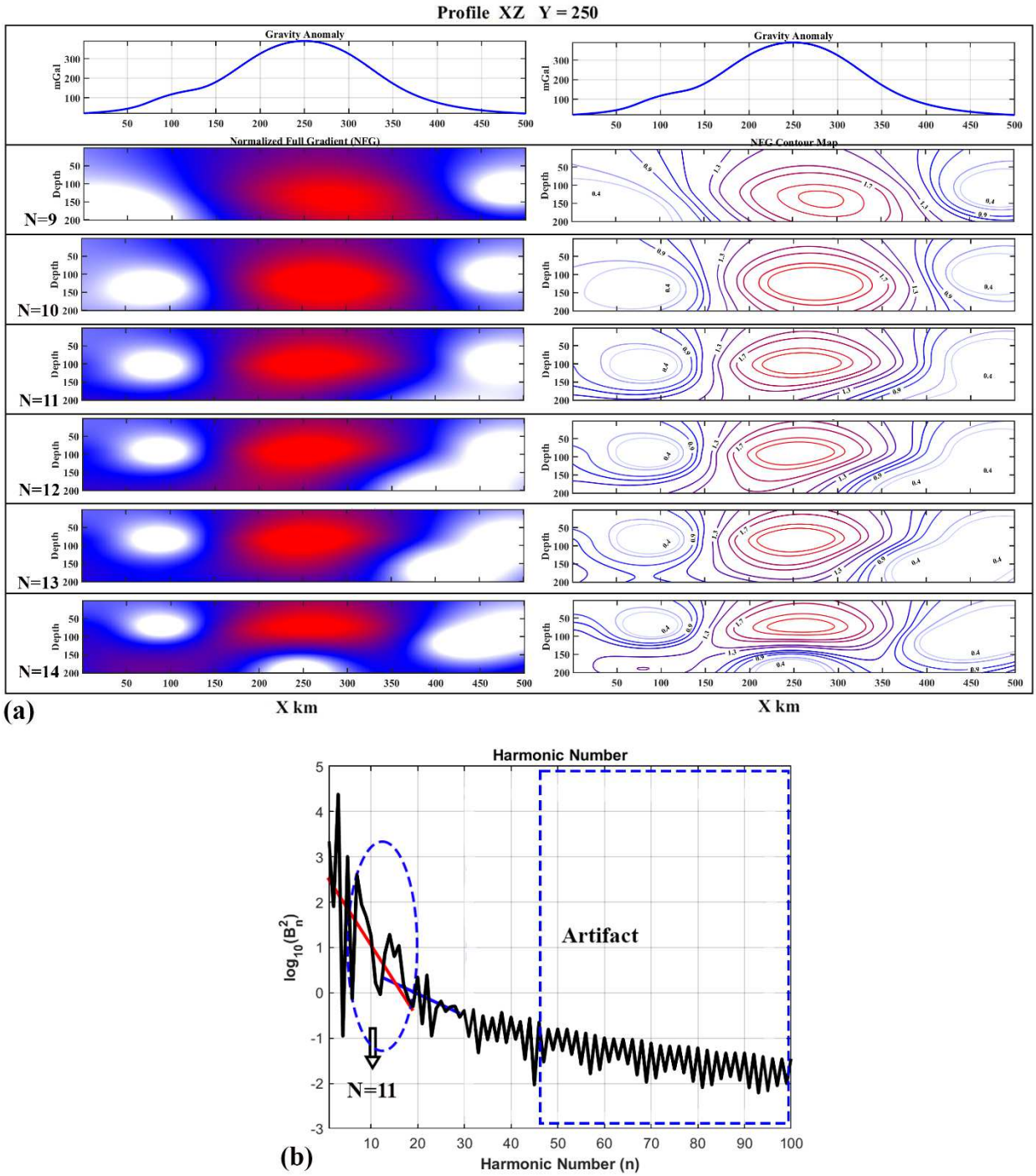


832

833 **Figure 6.** Vertical sections of the gravity anomaly, UCRD, and NFG responses for Synthetic Model 2

834 along (a) the XZ profile at Y = 250 km and (b) the YZ profile at X = 250 km. Figure conventions are as in

835 Figure 3.



836

837 **Figure 7.** (a) NFG responses along the XZ profile at Y = 250 km for harmonic numbers n = 9–14. The left

838 panels show color maps and the right panels show the corresponding contour representations. (b) Harmonic-

839 energy spectrum plotted as $log_{10}({B_n}^2)$ versus harmonic number n. The red line corresponds to the long-

wavelength (low-degree) harmonic regime, whereas the blue line represents the short-wavelength (high-degree) harmonic regime. The transition zone between the two trends indicates the optimal harmonic number (N = 11). The blue dashed rectangle outlines the artifact region excluded from interpretation.

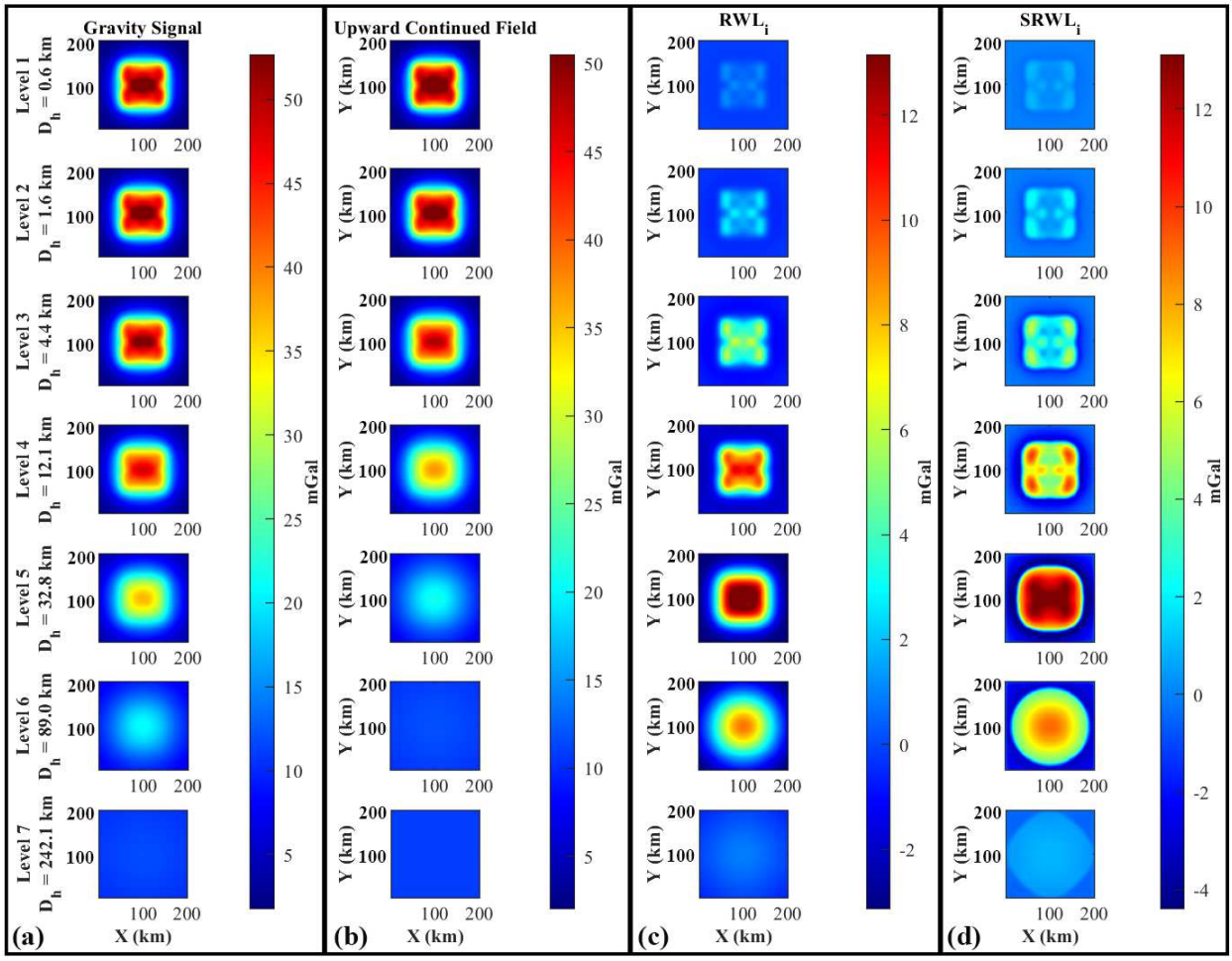
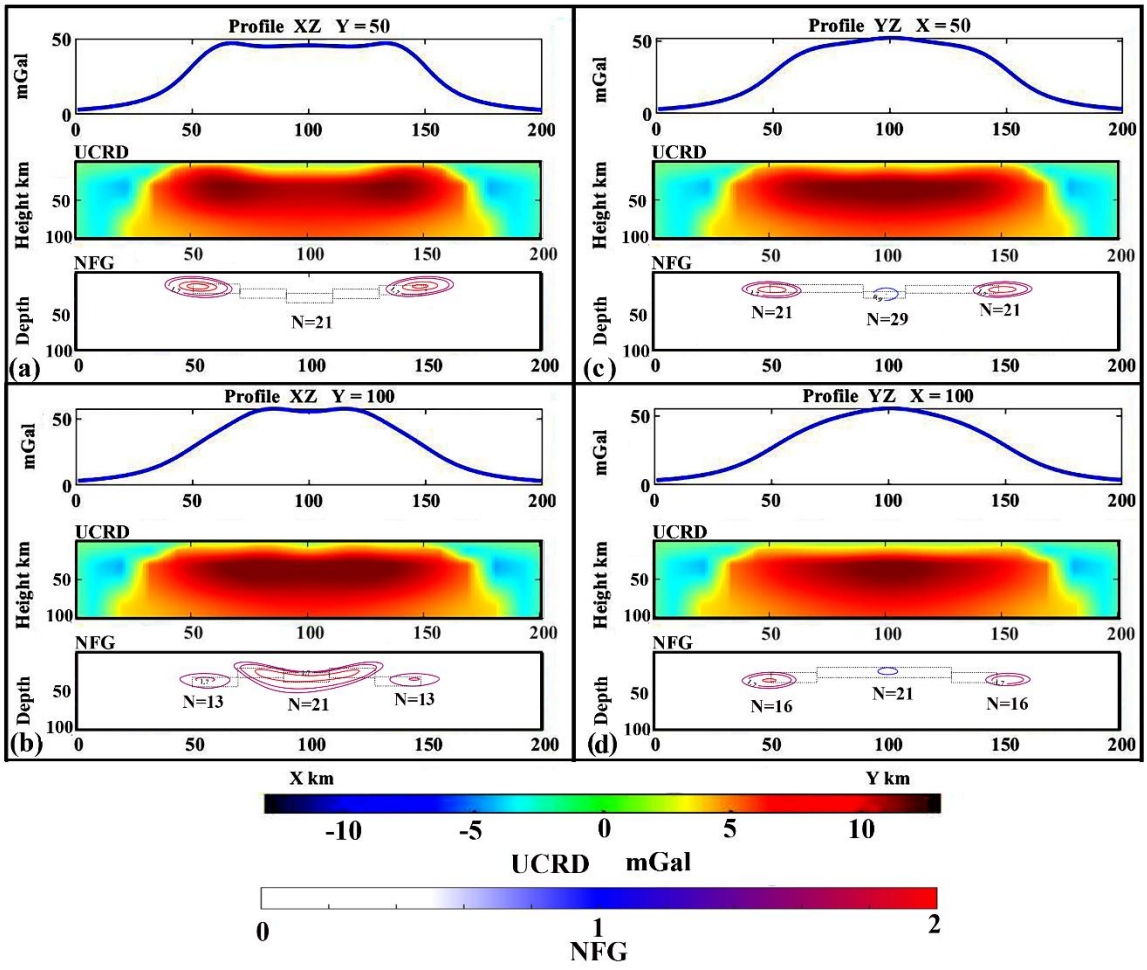


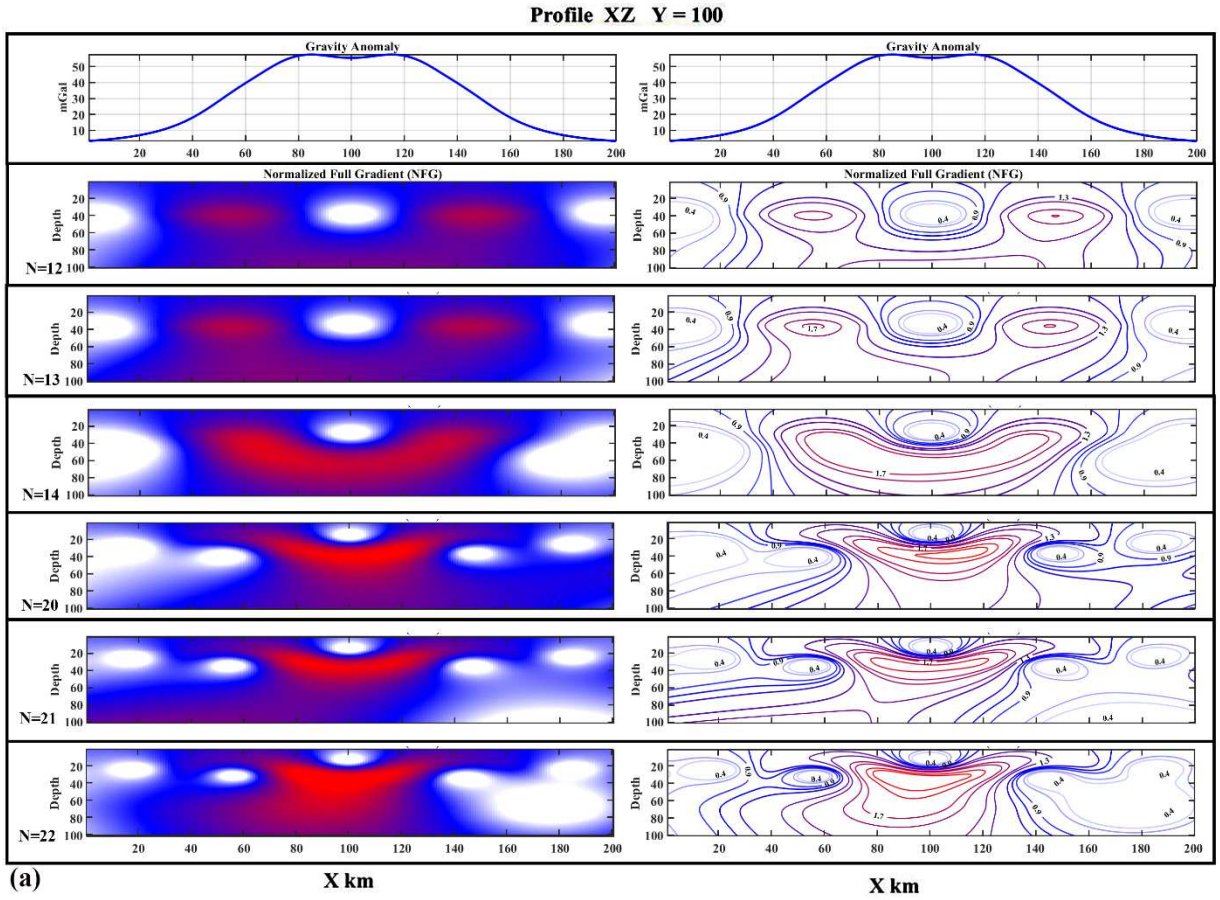
Figure 8. Step-by-step UCRD procedure for synthetic model 3 (Fig. 1c and Table 3). (a) Gravity signal, (b) upward continued field, (c) RWL_i, and (d) $SRWL_i$ at each UCRD level.

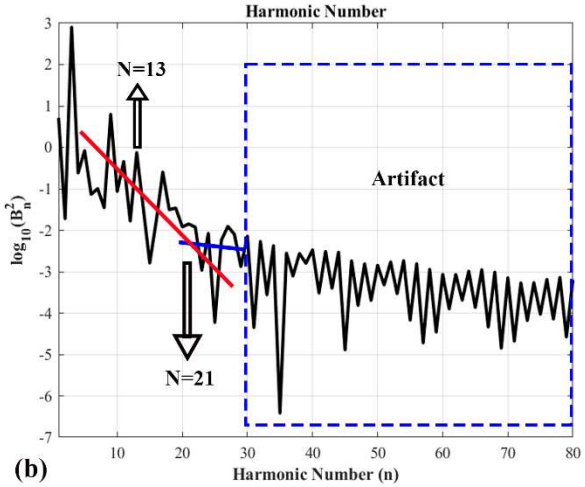


848

849 **Figure 9.** Vertical slices of the anomaly, UCRD, and NFG responses for synthetic model 3 along XZ

850 profiles at (a) Y = 50 km and (b) Y = 100 km, and along YZ profiles at (c) X = 50 km and (d) X = 100 km.





851

852 **Figure 10.** (a) NFG responses along the XZ profile at Y = 100 km for harmonic numbers n = 12–14 and n
853 = 20–22. The left panels show color maps and the right panels show the corresponding contour
854 representations. (b) Harmonic-energy spectrum plotted as $log_{10}({B_n}^2)$ versus harmonic number n. The red

line corresponds to the long-wavelength (low-degree) harmonic regime, whereas the blue line represents the short-wavelength (high-degree) harmonic regime. The transition between the two regimes occurs near N = 21, which provides the most stable response for interpretation. The blue dashed rectangle outlines the artifact region excluded from interpretation

Tables

Table 1. Properties of synthetic model 1 features (Fig. 1a).

Feature	Type	Density (kg/m³)	Depth Range (km)	Coordintes (X, Y)	Additional Notes
Cube 1	Cube	300	10–30	(300, 500)	
Cube 2	Cube	-600	40–80	(500, 500)	
Cube 3	Cube	400	20–70	(100, 300)	
Cube 4	Cube	600	40–80	(500, 300)	
Cube 5	Cube	-400	20–70	(100, 100)	
Cube 6	Cube	500	30–70	(300, 100)	
Stepped Block 1	Stepped Block	550	10–50	(500, 100)	Composed of four prisms, each 10 km thick
Near-Surface Block 1	Rectangular Prism	650	10–20	(500, 100)	Adjacent to Stepped Block 1
Stepped Block 2	Stepped Block	550	10–50	(100, 500)	Composed of four prisms, each 10 km thick
Near-Surface Block 2	Rectangular Prism	550	10–20	(100, 500)	Adjacent to Stepped Block 2
Stepped Block 3	Stepped Block	550	10–50	(300, 300)	Composed of four prisms, each 10 km thick

866 **Table 2.** Properties of synthetic model 2 (three rectangular prisms; see Fig. 1b).

Feature	Type	Density (kg/m^3)	Depth Range (km)	Additional Notes
Rectangular Prism 1	Rectangular Prism	300	20–30	Represents the shallowest structure
Rectangular Prism 2	Rectangular Prism	400	30–60	Intermediate-depth structure
Rectangular Prism 3	Rectangular Prism	500	50–100	Deepest structure
High-Density Overlap Zone	Overlapping Region	900	50–60	Overlap between prisms 2 and 3, with high-density anomaly

867

868 **Table 3.** Properties of synthetic model 3 features (Fig. 1c).

Feature	Type	Density (kg/m^3)	Depth Range (km)	Size (km)	Additional Notes
Block 1–25	Neighboring Blocks	200	10–30	20×20 in XY plane, 10 km thick	All blocks have the same density, buried at varying depths

869